

# Automatic Glare Detection via Photometric, Geometric, and Global Positioning Information

Mehran Andalibi, Department of Mechanical Engineering, Embry-Riddle Aeronautical University, Prescott, Arizona, USA  
Damon M. Chandler, Department of Electrical and Electronic Engineering, Shizuoka University, Hamamatsu, Shizuoka, Japan

## Abstract

Glare due to sunlight, moonlight, or other light sources can be a serious impediment during autonomous or manual driving. Automatically detecting the presence, location, and severity of such glare can be of critical importance for an autonomous driving system, which may then give greater priority to other sensors or cues/parts of the scene. We present an algorithm for automatic real-time glare detection that uses a combination of: (1) the intensity, saturation, and local contrast of the input frame; (2) shape detection; and (3) solar azimuth and elevation computed based on the position and heading information from the GPS (used under daylight conditions). These data are used to generate a glare occurrence map that indicates the center location(s) and extent(s) of the glare region(s). Testing on a variety of daytime and nighttime scenes demonstrates that the proposed system is effective at glare detection and is capable of real-time operation.

## Introduction

A very common occurrence during navigation is the presence of overly intense light that can overwhelm the driver or visual sensors of an autonomous ground vehicle, and thereby reduce visibility. When dazzled by a light source, typical reactions by the drivers are (1) flipping down the sunshades, which is not always effective, especially when the glare is caused by a low-positioned external light source, e.g., low sun or direct light from the headlights of the oncoming vehicle; (2) using one hand to occlude the strong light source from the eyes of the driver, which is not safe and can block the view of some important obstacles on the road; and (3) wearing sunglasses, which has comfort issues [1]. For autonomous vehicles which depend on onboard cameras for navigation, none of these reactions are possible, thus resulting in the partial or full loss of environment perception and subsequent failures.

Although the detection of glare is an important problem, there are relatively few publications on glare detection using digital cameras [2, 3, 4, 5, 1, 6]. The existing approaches to glare detection generally rely on one or two simplistic image properties, followed by ad-hoc thresholding. The obvious and most commonly used feature is light intensity [2, 3], which can certainly detect the light source(s), but which cannot differentiate these sources from other bright regions (e.g., clouds), as demonstrated in Figure 1.

To overcome this limitation, other approaches supplement intensity with hue, followed by spatial filtering or transformations [4, 5]. However, hue often fails to delineate the boundaries of the glare region(s), particularly when the image is subject to compression, as demonstrated in Figure 2. Instead of analyzing the scene, another class of approach has focused on analyzing an image of

the drivers face [1, 6]. Unfortunately, this approach cannot be used in autonomous systems nor in scenarios where the drivers environment is different from the actual to-be-driven location (e.g., in remote navigation).



**Figure 1.** Using light intensity alone to detect the glare regions also captures bright, non-glare regions: (a) Original image; (b) binarized intensity values using a threshold of 95% of the maximum value.

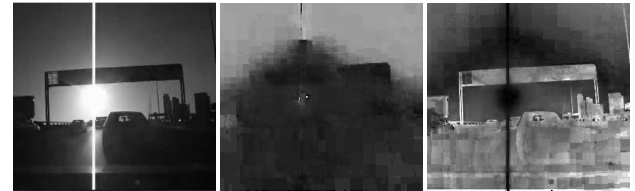


**Figure 2.** HSV color space components of an image with glare: (a) Intensity values (V channel); (b) hue values (H channel); (c) saturation values (S channel). Previous approaches have used intensity and hue; part of our approach uses intensity and saturation, the latter being more reliable at detecting the spatial extent of each glare region.

In this paper, we present an algorithm for glare detection that can reliably detect the presence of glare in both daytime and nighttime settings, and which can be used in autonomous or remote navigation settings (i.e., which does not rely on the analysis and co-presence of a human driver). Our approach employs an adaptive combination of features which remain computational simplistic, but which can reliably detect both the location(s) and extent(s) of the glare region(s). We specifically use a combination of: (1) the intensity, saturation, and local contrast of the input frame; (2) shape detection; and (3) solar azimuth and elevation computed based on the position and heading information from the GPS (used under daylight conditions). These data are used to generate a glare occurrence map that indicates the center location(s) and extent(s) of the glare region(s).

The main contributions of this work are as follows: Our approach is the first to use a combination of photometric, geometric, and GPS information to perform glare detection. For the photo-

metric approach, we propose a combination of lightness, saturation, and local contrast that performs more reliably than previous hue-based approaches, and which does not require facial analysis of the assumed co-located driver. We also propose a geometric approach by detecting circular regions within the preliminary glare occurrence map, which to the best of our knowledge has not been previously used for glare detection. Lastly, to the best of our knowledge, our approach is the first to make use of the sun's azimuth and elevation to further refine the localization process.

This paper is organized as follows. In the *Algorithm* section, we provide details of the algorithm. In the *Results* section, we evaluate and discuss the performance of the algorithm. The *Conclusions* section provides general conclusions and directions for future work.

## Algorithm

Our proposed algorithm operates by using four efficient image features along with GPS heading and position information (during daytime navigation). The input to the algorithm is a frame of the navigation video; the output is an equally sized map denoting the probability of glare at each spatial location. The algorithm operates independently on individual frames of the input video; no temporal input is used.

### Photometric Features

Each input frame (image) is assumed to contain RGB pixel values, where each of the R, G, and B color planes is represented by 8 bits/pixel. Let  $I$  denote this input image. The following three photometric features are then computed from  $I$ .

#### Intensity

Glare regions tend to be the brightest regions in an image, and thus light intensity can be a useful feature. We use the value component from the *HSV* color-space to obtain the grayscale intensity of each pixel. Let  $V$  denote the intensity map.  $V$  is computed as follows:

$$V(x, y) = \max_{x, y} \{I_R(x, y), I_G(x, y), I_B(x, y)\}, \quad (1)$$

where  $I_R$ ,  $I_G$ , and  $I_B$  denote the red, green, and blue channels of  $I$ .

Figures 3(b) and 4(b) show the resulting intensity maps for the example input images shown in Figures 3(a) and 4(a), respectively.

#### Saturation

Regions with very low color saturation are also good candidates of glare regions. We use the saturation component from the *HSV* color-space to obtain the color saturation of each pixel. Let  $S$  denote the saturation map.  $S$  is computed as follows:

$$S(x, y) = \begin{cases} \frac{V(x, y) - \min_{x, y} \{I_R(x, y), I_G(x, y), I_B(x, y)\}}{V(x, y)}, & \text{for } V(x, y) > 0 \\ 0, & \text{otherwise.} \end{cases} \quad (2)$$

Figures 3(c) and 4(c) show the resulting saturation maps for the example input images from Figures 3(a) and 4(a), respectively.

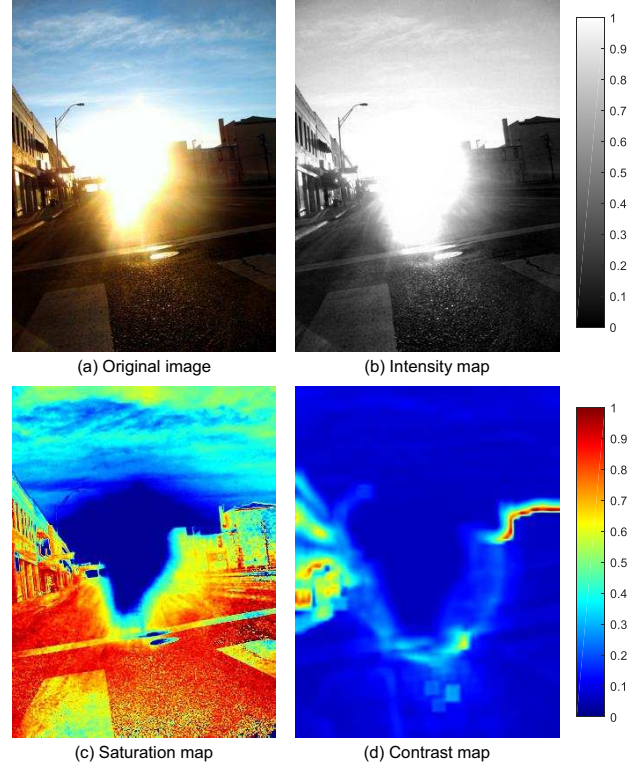


**Figure 3.** Original image (a) and the various photometric feature maps (b)-(d).

#### Local Contrast

Regions with very low luminance contrast are also good candidates of glare regions. To measure the local contrast, we first divide the image into overlapping blocks of size  $17 \times 17$  pixels (with 4 pixels of offset to the next block). Then, within each block, we measure the RMS contrast, given as the standard deviation of the luminance values of the block, divided by the mean of the luminance values of the block. Let  $C$  denote the contrast map.  $C$  is computed as follows:

$$C(x, y) = \frac{\sqrt{\frac{1}{288} \sum_{x', y'} [L(x', y') - \bar{L}(x, y)]^2}}{\max\{10, \bar{L}(x, y)\}}, \quad (3)$$

where  $L(x, y) = [0.02874 \times V(x, y)]^{2.2}$  denotes the estimated luminance in  $\text{cd/m}^2$  (assuming sRGB conditions); where  $\{x', y'\}$  denote the coordinates corresponding to the  $17 \times 17$  block centered at  $(x, y)$ ; and where  $\bar{L}(x, y)$  denotes the mean luminance of that block. We use a lower limit in the denominator of 10  $\text{cd/m}^2$  to avoid disproportionately large contrasts.

Note that  $C(x, y)$  is not computed for every  $(x, y)$  but only for every fourth coordinate. The remaining values are filled in via pixel replication in order to obtain a map that is equal in size to the other maps.

Figures 3(d) and 4(d) show the resulting contrast maps for the example input images from Figures 3(a) and 4(a), respectively.

#### Overall Photometric Map

The intensity, saturation, and contrast maps are combined into a single photometric-based glare occurrence map,  $G_{photo}$ , as

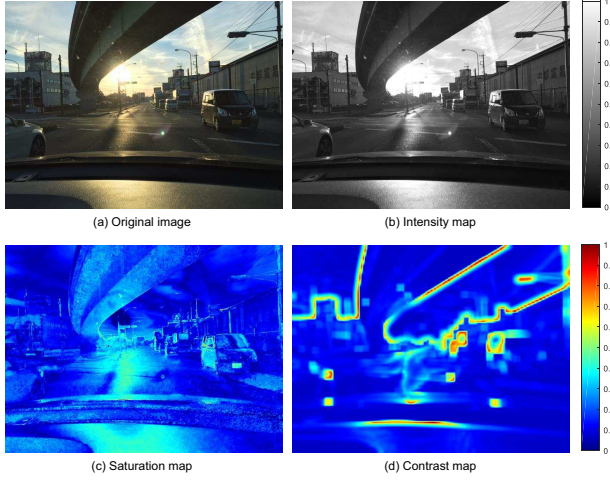


**Figure 4.** Original image (a) and the various photometric feature maps (b)-(d).

follows:

$$G_{photo}(x,y) = I(x,y) \times (1 - S(x,y)) \times (1 - C(x,y)), \quad (4)$$

followed by normalization to span the range  $[0, 1]$ . Thus, regions of high light intensity, low color saturation, and low luminance contrast are estimated to be the most likely candidates of glare regions.

Figure 5(b) shows an example GPS-based glare occurrence map for the input image in Figure 5(a). Additional maps are shown later in Figure 6.

### Geometric Feature

In addition to photometric properties, sources of glare can have distinct geometric cues: (1) the sources tend to be circular, and (2) the sources sometimes exhibit rays which emanate from the center of each source. Unfortunately, the rays are subtle, and therefore difficult to detect reliably without significant computation. However, circular shapes can be detected relatively quickly and with reasonable accuracy by using Hough-transform-based methods.

Thus, for our geometric feature, we detect circles. We specifically employ the Hough-transform-based algorithm from [7], applied to a Gaussian-blurred version of the  $G_{photo}(x,y)$  map. The circle-detection algorithm is used to search for circles with radii from 10-200 pixels. The Gaussian filtering is used to remove noise; we use a filter size of  $15 \times 15$  pixels with a standard deviation of 5 pixels. The algorithm from [7] yields both the center locations and the radii of the detected circles. We generate our geometric-based glare occurrence map,  $G_{geo}$ , from these data by using a mixture of Gaussians.

Let  $\{(x_i, y_i)\}$  and  $\{r_i\}$ ,  $i = 1, \dots, N$ , denote the sets of detected circle center points and radii, respectively. Let  $C_i$  denote an otherwise zero-valued map (of the same dimensions as the input image and  $G_{photo}$ ) with a single Gaussian blob with a standard deviation of  $1.5r_i$  and centered at  $(x_i, y_i)$ .  $G_{geo}$  is then generated as follows:

$$G_{geo}(x,y) = \frac{1}{N} \sum_{i=1}^N C_i(x,y), \quad (5)$$

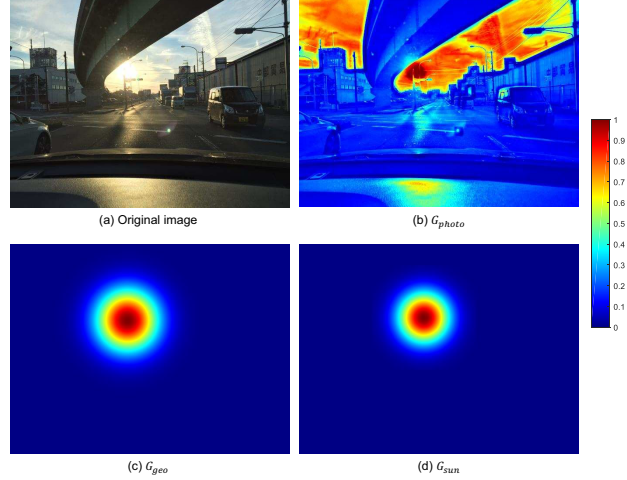


**Figure 5.** Original image (a) and the various glare occurrence maps (b)-(d).

followed by normalization to span the range  $[0, 1]$ .

Figure 5(c) shows an example geometric-based glare occurrence map for the input image in Figure 5(a). Additional maps are shown later in Figure 6.

### Global Positioning Information

During daytime conditions, the main source of glare is the sun. If the sun is covered partially by clouds, the glare regions detected using the aforementioned features would be erroneously larger than the true glare source. However, when GPS information is accessible, the time, date, latitude, longitude, elevation, and heading of the vehicle/camera can be acquired. By using the latitude, longitude, time, and date, the solar azimuth and elevation can be calculated. This azimuth and elevation can then be used in conjunction with the vehicle heading and the road slope (which are also measurable from GPS data) to determine the position of the sun within the frame.

We denote the sun's elevation and azimuth angles by  $h$  and  $A$ , the heading with respect to North by  $hd$ , the camera horizontal and vertical fields of view by  $HFOV$  and  $VFOV$ , and the road slope angle by  $sp$ . The road slope angle can be determined from the vehicle's elevation readings followed by a linear least-squares curve fitting:

$$sp = \frac{\sum_1^5 d_i e_i - 5\bar{d}\bar{e}}{\sum_1^5 d_i^2 - 5\bar{d}^2}, \quad (6)$$

where  $e_i$  and  $d_i$  are the elevation and traveled distance readings (w.r.t. to a start point) and  $\bar{d}$  and  $\bar{e}$  are the average values of the last five readings of elevation and traveled distance.

The sun appears in the image if the follows conditions are satisfied:

$$h - sp < VFOV/2 \text{ and } A - hd < HFOV/2. \quad (7)$$

The x and y image coordinates of the suns center can be calculated via:

$$x_{sun} = 1 + \text{round}(W/2[1 + (h - sp)/(HFOV/2)]) \quad (8)$$

$$y_{sun} = 1 + \text{round}(H/2[1 - (A - hd)/(VFOV/2)]) \quad (9)$$

where  $W$  and  $H$  denote the width and height of the image.

If the sun is partially occluded by clouds or other white objects, the pixels surrounding the sun might be considered as belonging to the glare region. To assist this and related conditions, we generate a GPS-based glare occurrence map, denoted by  $G_{sun}$ , which is based on  $(x_{sun}, y_{sun})$ , and which is used only during daytime conditions. Specifically,  $G_{sun}$  is an otherwise blank image containing a single Gaussian kernel centered at  $(x_{sun}, y_{sun})$  and with a properly chosen kernel size. (In our present implementation, we use a fixed Gaussian standard deviation of 1/12th of the image's height.)

Figure 5(d) shows an example GPS-based glare occurrence map for the input image in Figure 5(a). Additional maps are shown later in Figure 6.

### Overall Glare Occurrence Map

In summary, good candidates for glare regions exhibit high light intensity, low color saturation, and low luminance contrast; this fact is captured by  $G_{photo}$ . Sources of glare tend to be circular in shape, a fact captured by  $G_{geo}$ . Furthermore, during the daytime, and assuming the availability of GPS information, the sun's position within the image can be used  $G_{sun}$  to estimate the location of the dominant glare source.

The requirements of each particular navigation setting will dictate the proper way to use and/or combine the maps. In an autonomous navigation setting, one reasonable goal would be mitigate the effects of the glare by selectively darkening the glare regions either digitally or physically. In this case, the location, extent, and intensity of each glare region is needed.  $G_{photo}$  and  $G_{geo}$  can provide this information; and these maps can further be combined with  $G_{sun}$  to, for example, completely obscure the sun from the imaging sensor.

Still, from an investigative standpoint, it is useful to explore simple combination rules. In the following section, we test and analyze two simplest combination rules for the three maps: a weighted average, and a weighted product.

## Results

### Qualitative Results

Figure 6 shows representative results of the proposed technique on various images taken from a driver's viewpoint. The first column shows the original images. The second through fourth columns show the individual maps  $G_{photo}$ ,  $G_{geo}$ , and  $G_{sun}$ . The remaining columns shows maps generated via the following combination rules:

**If  $G_{sun}$  is available:**

$$G_{mean} = \frac{3}{4}G_{photo} + \frac{1}{8}G_{geo} + \frac{1}{8}G_{sun}. \quad (10)$$

$$G_{prod} = G_{photo} \times (\frac{3}{4} + \frac{1}{8}G_{geo} + \frac{1}{8}G_{sun}). \quad (11)$$

**If  $G_{sun}$  is not available:**

$$G_{mean} = \frac{1}{2}G_{photo} + \frac{1}{2}G_{geo}. \quad (12)$$

$$G_{prod} = G_{photo} \times (\frac{1}{2} + \frac{1}{2}G_{geo}). \quad (13)$$

Note that these are all pointwise operations performed on individual pixels of the maps. For  $G_{prod}$ , because  $G_{sun}$  contains only the detected sun location,  $G_{sun}$  is scaled and offset to prevent elimination of glare due to reflections.  $G_{geo}$  is similarly scaled and offset so as not to eliminate potential glare regions that are non-circular

or otherwise undetected by the geometric analysis. The weights for  $G_{mean}$  were selected for these same reasons.

Observe from Figure 6 that the proposed technique is quite effective at detecting the glare regions.  $G_{prod}$  and  $G_{mean}$  both appear to yield reasonably accurate detection results; however, observe that  $G_{mean}$  tends to be a bit more liberal than  $G_{prod}$  (e.g., above the sun in the third image, and around the left lights in the fourth image).

### Quantitative Results

We tested the proposed algorithm of a small dataset of 10 images (nine daytime images, and one nighttime image) of size  $640 \times 480$  pixels. GPS and date/time information was available only for five of the images. To quantify the predictive performance, we used F-measure as region-based criteria for evaluation, and we used Boundary Displacement Error (BDE) as a boundary-based criterion.

Given a ground-truth binary glare map  $GT$  and a detected binary glare map  $DT$ , the F-measure is computed via:

$$F_\alpha = \frac{(1 + \alpha) \times Precision \times Recall}{\alpha \times Precision + Recall}, \quad (14)$$

where Precision and Recall are given as follows:

$$Precision = \frac{A(D \cap G)}{A(D)}, \quad (15)$$

$$Recall = \frac{A(D \cap G)}{A(G)}, \quad (16)$$

where the  $A(\cdot)$  operator computes the area of a region. In this paper, we used a value of  $\alpha = 0.5$ . The ground-truth binary glare maps ( $GT$  maps) were generated via hand-segmentation by the first author. The detected binary glare maps ( $DT$  maps) were generated from  $G_{photo}$  by using a threshold of 0.9, and from  $G_{prod}$  and  $G_{sun}$  by using a threshold of 0.85.

The BDE measures the average displacement error between the boundaries of two regions. Let  $B_D$  and  $B_G$  represent the boundary point set of the detected and ground truth regions, respectively. The BDE from  $B_D$  to  $B_G$ , denoted as  $E(D, G)$ , is computed as the average of distances from every point  $p$  in  $B_D$  to  $B_G$ :

$$E(D, G) = \frac{1}{|B_D|} \sum_{p \in B_D} d(p, B_G), \quad (17)$$

where  $|B_D|$  represents the number of points in set  $B_D$  and  $d(p, B_G)$  represents the minimum Euclidean distance from  $p$  to all points in  $B_G$ :

$$d(p, B_G) = \min_{q \in B_G} \{\sqrt{(p_1 - q_1)^2 + (p_2 - q_2)^2}\},$$

where  $(p_1, p_2)$  and  $(q_1, q_2)$  are coordinates of  $p$  and  $q$ , respectively.

The BDE from  $B_G$  to  $B_D$ , denoted as  $E(G, D)$ , is computed similarly. The final BDE between  $B_D$  and  $B_G$  is therefore computed as the average of these two BDEs:

$$BDE(B_D, B_G) = \frac{1}{2}(E(D, G) + E(G, D)). \quad (18)$$



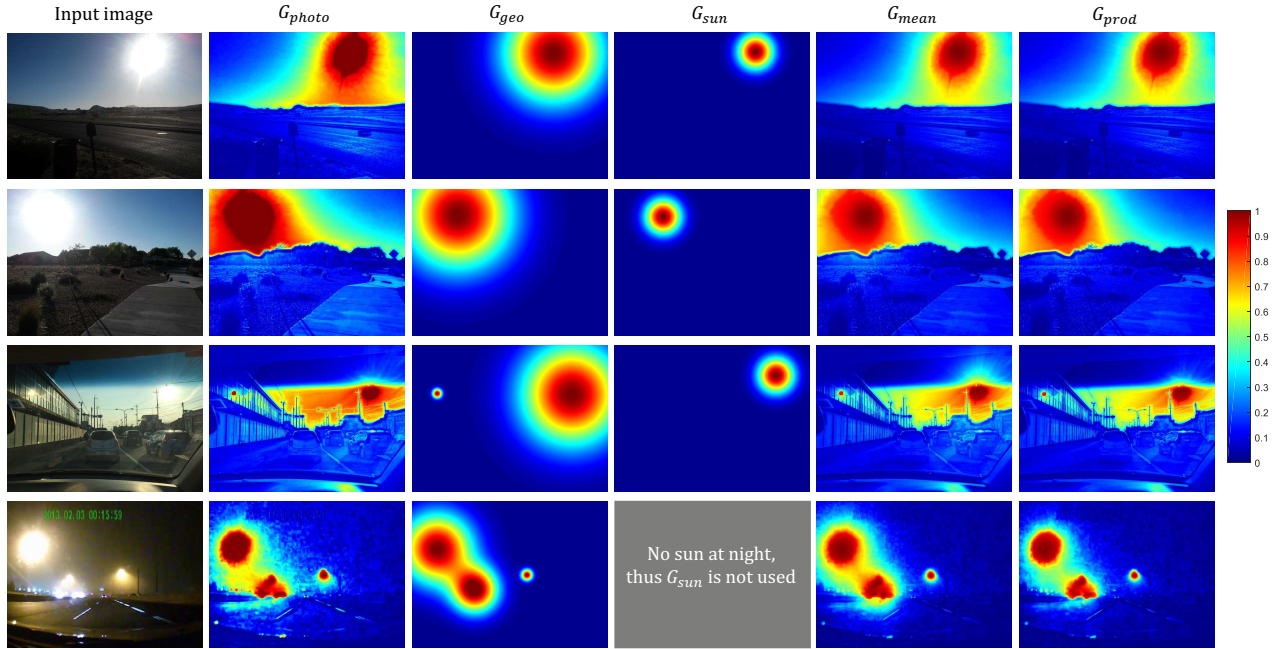


Figure 6. Representative results of the proposed algorithm; see text for details.

Table 1: F-measure and BDE for the 10 test images.

	F-measure			BDE		
	$G_{photo}$	$G_{mean}$	$G_{prod}$	$G_{photo}$	$G_{mean}$	$G_{prod}$
Image 1	0.918	<b>0.973</b>	<b>0.973</b>	1.7	<b>0.1</b>	1.8
Image 2	0.760	0.944	<b>0.949</b>	2.0	<b>0.2</b>	1.4
Image 3	0.655	<b>0.684</b>	0.660	25.3	<b>17.7</b>	26.6
Image 4	0.961	<b>0.973</b>	0.968	26.7	<b>16.5</b>	26.5
Image 5	<b>0.930</b>	0.866	0.912	29.8	<b>19.1</b>	29.2
Image 6	0.675	0.703	<b>0.714</b>	39.8	<b>27.4</b>	37.6
Image 7	0.958	0.937	<b>0.977</b>	1.2	<b>0.1</b>	1.3
Image 8	0.790	<b>0.843</b>	0.811	6.7	<b>2.0</b>	6.1
Image 9	0.850	0.823	<b>0.874</b>	<b>1.3</b>	2.0	1.8
Image 10	<b>0.871</b>	0.822	0.826	6.0	<b>4.6</b>	6.3
Average	<b>0.837</b>	<b>0.866</b>	<b>0.857</b>	<b>14.0</b>	<b>13.9</b>	<b>9.0</b>

The results of these measures are shown in Table 1. Note that GPS and date/time information were unavailable for the latter five images, and *Image 10* was the single nighttime image. Overall, the results are quite promising. In all but two cases, the use of geometric and GPS information can improve the photometric-only results. These data also demonstrate that  $G_{mean}$  is better choice if the goal is to more accurately detect the boundaries of the glare regions.

## Conclusions

In this paper, we presented a new method for detecting the location and extent of glare regions captured by moving vehicles' onboard cameras using photometric, geometric, and global positioning information. Among these features, photometric information can be used for both daytime and nighttime sequences all the times; global positioning information detects the sun glare in all daytime conditions and can limit the size of the glare region, es-

pecially if the sun is occluded by bright objects, such as white clouds; and geometric information seems to be promising for further assisting the detection process. The accuracy of the method, evaluated using qualitative results and quantitative measures, was relatively high.

Although we have not reported the runtime performance of the method, for the  $640 \times 480$  images used in this study, the average runtime is under 40 ms per image on a 3.2 GHz i7-970 workstation using a basic OpenCV implementation. A full performance analysis is part of our future work.

## References

- [1] X. Liu, A. Leu, D. Bacara, M. Hainfellner, and A. Graeser, "Robust dazzling detection in a novel visual based dazzling avoidance system," in *2014 IEEE Intelligent Vehicles Symposium Proceedings*. IEEE, 2014, pp. 833–838.
- [2] S. Pharadornpanitchakul and R. Chaisrichaen, "Danger detection from head light glare through vision estimation," in *Communications and Information Technologies (ISCIT), 2013 13th International Symposium on*. IEEE, 2013, pp. 661–664.
- [3] M. Shehata, M. Pervez, J. Cai, and W. B. A. Radmanesh, "Real time static glare identification in its," *Practical Real World Technologies for Communications and Embedded Platforms*, 2006.
- [4] C.-S. Cho, J. Song, and J.-I. Park, "Glare region detection in night scene using multi-layering," in *The Third International Conference on Digital Information Processing and Communications*. The Society of Digital Information and Wireless Communication, 2013, pp. 467–469.
- [5] H. Kumon and M. Haseyama, "Glare detection for night wet road surfaces and driver visibility improvement by using multiple onboard cameras," *The Journal of the Institute of Televi-*

- sion Engineers of Japan, vol. 67, no. 3, pp. J95–J103, 2013.
- [6] D. Aiteanu, J. Zeisler, and M. Hainfellner, “Selective darkening of the windshield using high speed video analysis for driving assistance,” in *Optimization of Electrical and Electronic Equipment (OPTIM), 2012 13th International Conference on*. IEEE, 2012, pp. 1465–1470.
- [7] T. Atherton and D. Kerbyson, “Size invariant circle detection,” *Image and Vision Computing*, vol. 17, no. 11, pp. 795 – 803, 1999.

## Author Biography

*Mehran Andalibi received his Ph.D. degree in Mechanical Engineering from Oklahoma State University, U.S.A. in 2014. He is currently an Assistant Professor in the Department of Mechanical Engineering, Embry-Riddle Aeronautical University, AZ, U.S.A. His research interests are the application of computer vision in intelligent machines, including vision-based navigation of autonomous ground robots, early detection of wildfire using unmanned aircraft and image processing, and vision-based robotic-assisted surgery.*

*Damon Chandler received his Ph.D. degrees in Electrical engineering from Cornell University, Ithaca, NY, in 2005. From 2006 to 2015, he was on the faculty of the School of Electrical and Computer Engineering, Oklahoma State University, U.S.A. He is currently an Associate Professor in the Department of Electrical and Electronic Engineering, Shizuoka University, Japan. His research interests include image processing, data compression, computational vision, natural scene statistics, and visual perception.*